Neuron, Volume *80*

Supplemental Information

Balanced Synaptic Impact through Distance-Dependent Synapse Distribution and Complementary Expression of AMPA and NMDA Receptors in Hippocampal Dendrites

Vilas Menon, Timothy F. Musial, Annie Liu, Yael Katz, William L. Kath, Nelson Spruston, and Daniel A. Nicholson

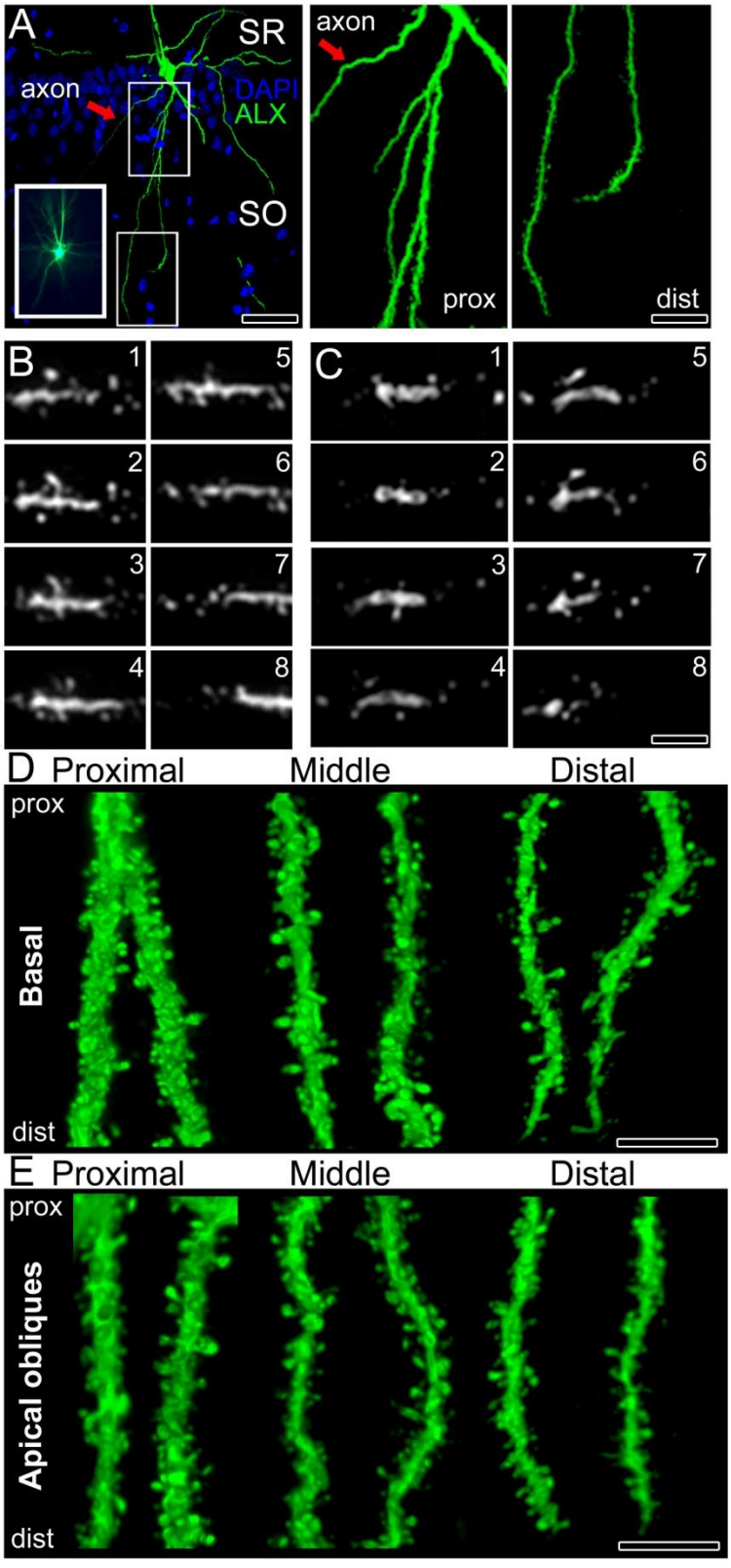

Figure S1. Reconstructed dendrites using array tomography. Array tomography of single dendrites support the electron microscopic analyses, with apparent numerical scaling among spines and tapering dendritic diameters in both basal and apical oblique dendrites.
A) *Left* Partial rendering of a dye-injected CA1 pyramidal neuron and its dendrites from 573 serial sections. Inset in lower left is a fluorescence image of the LR white-embedded neuron (before sectioning). White boxes

in proximal and distal stratum oriens (SO) are shown at higher magnification in the two *Right* panels, respectively. SR = stratum radiatum. DAPI = blue; Alexa Fluor 488 (ALX) = green. Scale bars = 50 and 15 μm.
B,C) Fluorescence images of a filled dendrite and its spines from serial sections within an array. Scale bar = 1 μm.
D) Representative renderings of individual dendritic segments from proximal, middle, or distal SO. Scale bar = 3 μm. Portions of each dendrite at the bottom correspond to the most distal portion of each segment (nearest the alveus); portions at the top are proximal portions (nearest the soma).
E) Representative renderings of individual dendritic segments from apical oblique dendrites in stratum radiatum, corresponding to locations proximal to the branch point off of the main apical dendrite (proximal), in the middle of the dendrite (middle), or nearest their terminal ends (distal). Scale bar = 3 μm. Portions of each dendrite at the bottom correspond to the most distal portion of each segment (nearest the terminal end); portions at the top are proximal portions (nearest the branch point off of the apical dendrite).

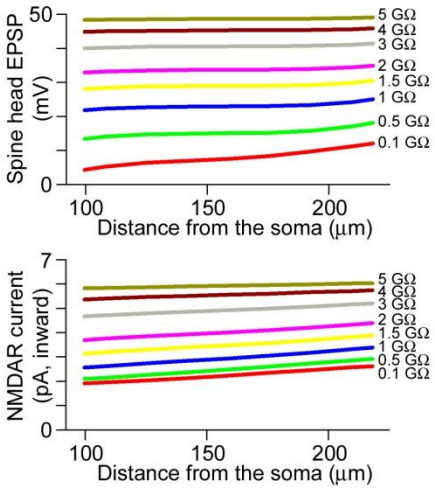

Figure S2 Effects of spine neck resistance on spine head voltage and peak NMDAR-mediated inward current

Top Spine head EPSP as a function of dendritic position and spine neck resistance. Spine neck resistances were held constant for each round of simulations, ranging from 0.1 to 5 GΩ.

Bottom Peak NMDAR-mediated current in the spine head as a function of dendritic position and spine neck resistance. Spine neck resistances range from 0.1 to 5 GΩ. For both panels, the values along the abscissa correspond to the spine location on the same dendrite for all simulations, such that values on the left are closest to the branch point and values on the right are closest to the dendrite's terminal end.

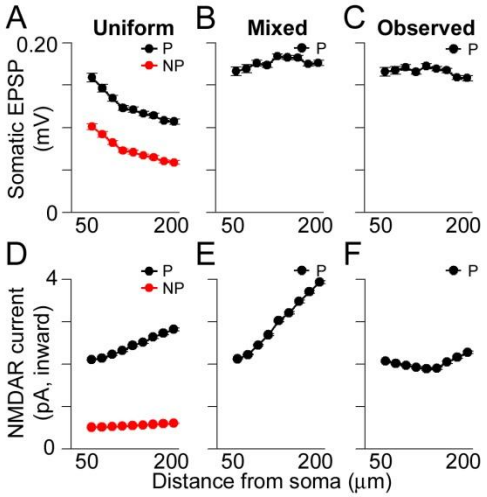

Figure S3 Location-independent contribution of individual perforated synapses to sub-threshold somatic voltage, with active Na^+ and A-type K^+ currents in spines. Na+-conductance was set at 0.03 S/cm^2, and was kept constant for all dendritic locations. A-type K+-conductance was set at 0.14 S/cm^2, and was kept constant for all dendritic locations.

A) Average amplitudes of simulated unitary somatic EPSPs in response to activated perforated (black) and nonperforated (red) synaptic conductances at various distances from the soma using uniform parameters.

B) Average amplitudes of simulated unitary somatic EPSPs in response to activated perforated synaptic conductances at various distances from the soma using the mixed conductance values.

C) Average amplitudes of simulated unitary somatic EPSPs in response to activated perforated synaptic conductances scaled according to experimentally observed AMPAR and NMDAR expression.

D-F) Peak NMDAR-mediated current in the spine head for the uniform (D), mixed (E), or experimentally observed (F) conductance simulations.

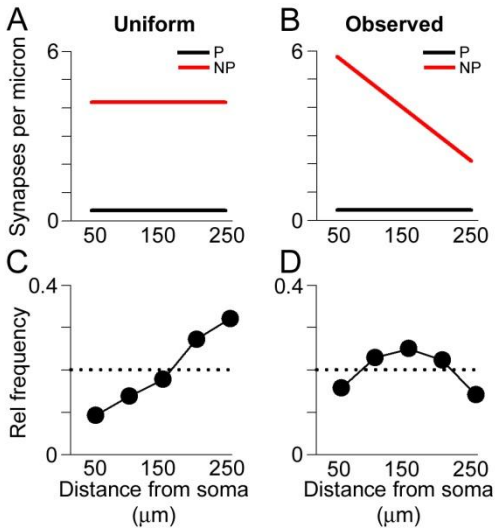

Figure S4 Location-independent contribution of synapses to dendritic spike initiation, with active Na^+ and A-type K^+ currents in spines. Na+-conductance was set at 0.03 S/cm^2, and was kept constant for all dendritic locations. A-type K+-conductance was set at 0.14 S/cm^2, and was kept constant for all dendritic locations.

A) Synapse density per unit length of dendrite in the uniform case for simulated perforated (black) and nonperforated (red) synapses.

B) Synapse density scaled according to experimentally observed values.

C) Plot showing the relative probability that a dendritic spike is generated by a synapse placed at a given location along the length of an individual dendrite, using the uniform conductance values shown in Figure 4B and uniform synapse densities shown in (A). Data are aggregated from 900 simulations containing both perforated and nonperforated synapses. The dashed line represents the uniform, or completely distance-independent, probability.

D) Same as (C), but with experimentally observed synaptic conductance values (Figure 4F) and synapse densities (B).

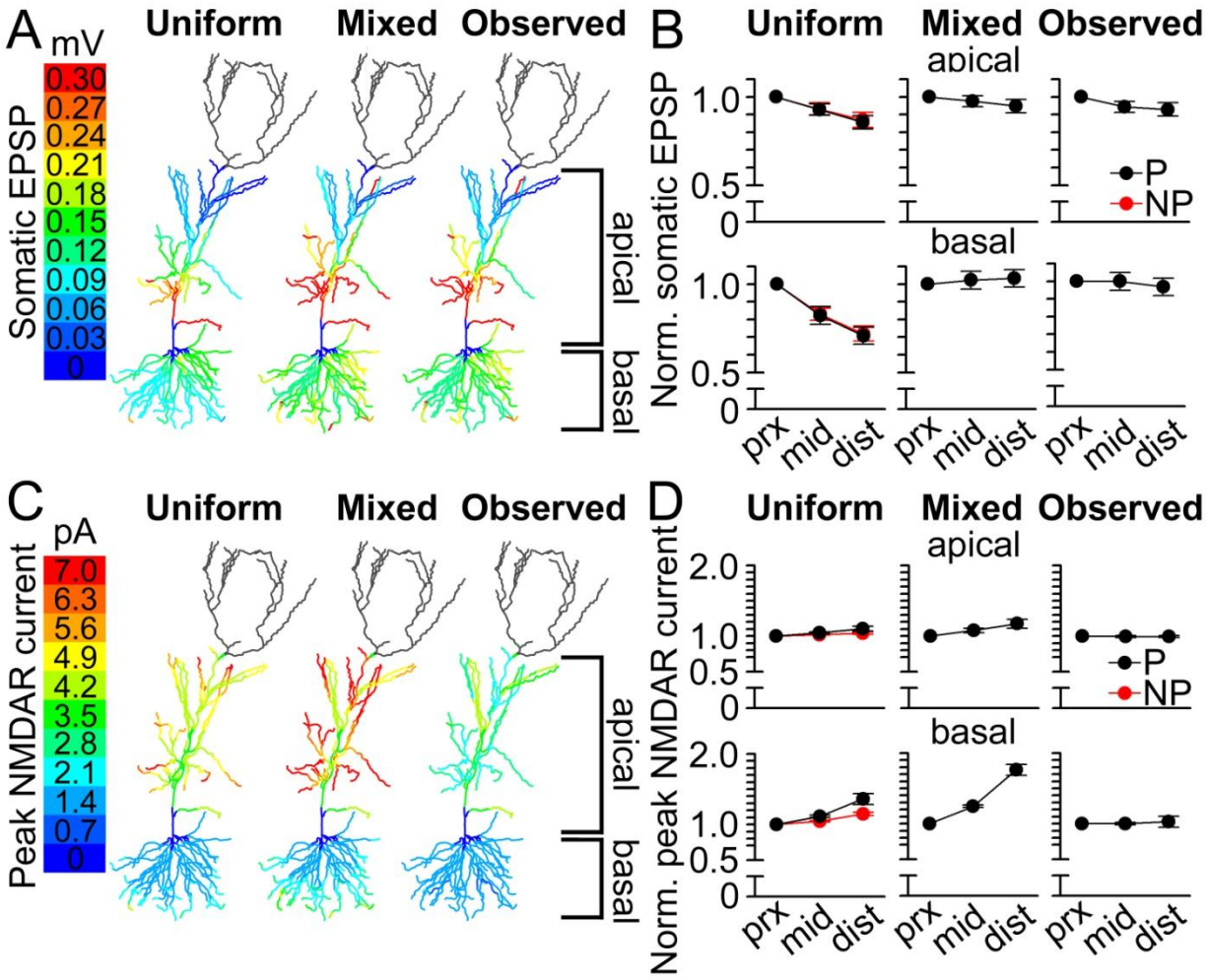

Figure S5 Simulations of single-dendrite ion channel gradients using dendritic diameters obtained from the electron microscopy experiments

A) Color-coded plots projected onto a morphologically realistic model hippocampal CA1 pyramidal neuron, showing the somatic EPSP generated in response to activated synaptic conductances at perforated synapses with three different patterns of AMPAR- and NMDAR-mediated conductances. In the uniform case (left), conductances were the same as depicted in Figure 4B. In the mixed case, AMPAR-mediated conductances were scaled according to dendritic diameter as shown in Figure 6C. In the observed case, both AMPAR-mediated and NMDAR-mediated conductances were scaled according to diameter as shown in Figure 6C. The dendrites of the apical tuft were not simulated, and are therefore darkened.

B) Average normalized amplitudes (normalized to the proximal third of each individual dendrite) of simulated unitary somatic EPSPs in response to activated perforated (black) and nonperforated (red) synaptic conductances at various distances from the soma using uniform (left), mixed (middle), or observed (right) parameters for apical oblique dendrites (top row) or basal dendrites (bottom row).

C) Color-coded plots projected onto a morphologically realistic model hippocampal CA1 pyramidal neuron, showing the peak NMDAR-mediated current (inward) to activated synaptic conductances at perforated synapses with three different patterns of AMPAR- and NMDAR-mediated conductances. In the uniform case (left), conductances were the same as depicted in Figure 4B. In the mixed case, AMPAR-mediated conductances were scaled according to dendritic diameter as shown in Figure 6C. In the observed case, both AMPAR-mediated and NMDAR-mediated conductances were scaled according to diameter as shown in Figure 6C. The dendrites of the apical tuft were not simulated, and so are darkened.

D) Average normalized peak NMDAR-mediated currents (normalized to the proximal third of each individual dendrite) in response to activated perforated (black) and nonperforated (red) synaptic conductances at various distances from the soma using uniform (left), mixed (middle), or observed (right) parameters for apical oblique dendrites (top row) or basal dendrites (bottom row).

Supplemental Experimental Procedures

Electron microscopy with BDA-labelling

Two young adult (6-month-old) male F1 hybrid Fischer344 x Brown Norway rats (Harlan, Indianapolis, Indiana) were anesthetized with an injection of ketamine and xylazine. Biotinylated dextran amine (BDA-3000, Invitrogen; 10% dissolved in 0.12 M phosphate buffered saline; PBS) was injected into the subiculum (from bregma: AP=-2.5, ML=+1.5, DV=-4.1) using pressure injection (0.05 mL/min for 5 min). After five days of recovery, rats were perfused with a mixture of paraformaldehyde, glutaraldehyde, and picric acid. Brains were removed, hemisectioned, postfixed, and sectioned into 60 μm thick slices.

Individual slices were cryoprotected in ascending concentrations of sucrose and glycerol solutions, freeze-thawed over liquid nitrogen, treated with 1% sodium borohydride, and incubated in 0.3% hydrogen peroxide. Slices were rinsed and incubated in avidin-biotinylated horseradish peroxide (HRP) using the Vectastain ABC Elite Kit (Vector Laboratories, PK-6100 Standard, 1:300). The BDA-HRP complex was visualized using diaminobenzidine as chromogen (Sigma, SK-4100). Slices containing isolated individually labeled CA1 pyramidal neurons were treated with osmium tetroxide and uranyl acetate, dehydrated in graded ethanols, infiltrated with Araldite (Araldite 502), and cured at 60˚C. Slices were trimmed to isolate labeled CA1 neuron dendrites and cut into serial ultrathin (67 nm) sections, which were then used to obtain mosaics of electron micrographs of dendritic segments. Dendritic segments near branch tips in dSO were considered to be those that could be followed through >50 serial sections before disappearing in subsequent serial sections, and whose ends were greater than 100 μm from the soma. Dendritic segments in pSO were easily identifiable due their direct attachment to the soma. The data comprised 7 total dendritic segments (4 in pSO and 3 in dSO). Of these, there were two pairs of within-branch segments (pSO and dSO segments from the same branch), and three isolated segments. The analysis included 364 axospinous synapses and 266 identifiable PSDs.

Electron micrograph negatives were scanned using an Epson 10000XL scanner, organized into image stacks of mosaics for each branch segment, and analyzed and reconstructed using ImageJ (Rasband, 1997-2007), and Reconstruct (Fiala, 2005) respectively.

Array Tomography

One young adult (6 months old) male F1 hybrid Fisher344xBrown Norway rat (Harlan, Indianapolis, IN) was perfused with 90 ml of 4% paraformaldehyde, after which the brain was removed, post-fixed in perfusate, and sectioned into 300 μm-thick slices. Hippocampal CA1 pyramidal neurons were dye-loaded with 10 mM Alexa Fluor 488 (Molecular Probes, Eugene, OR) dissolved in 200mM KCl under visual inspection using iontophoresis (10-15 nA negative current, 20 msec on/off) through a 150 MΩ microelectrode until brightly fluorescent. Slices were post-fixed in perfusate for 1 hour, and then microwave processed with a Pelco BioWave Pro (Ted Pella, Inc., Redding, CA) following Micheva et al. (2010), and embedded in LR White. Microwave processing was necessary to preserve the bright fluorescence of dye-loaded neurons and dendrites (see also Ferris et al. (2009)).

Twenty ribbons/arrays of 95-225 serial sections each (75 nm thick) were transferred onto gelatin-subbed coverslips, mounted with a DAPI-containing fluorescence-preserving medium (Vectashield, Vector Laboratories), and imaged with an AxioImager.M2 imaging system with an Axiocam MRm Digital Camera and AxioVision software (Carl Zeiss MicroImaging, LLC, Thornwood, NY). Candidate dendrites were visually identified while scrolling through the arrays, and were imaged if they were completely contained within the arrays. Coordinate systems were created with MosaicPlanner (generously provided by Dr. Stephen Smith, Stanford University), and images were acquired using a Zeiss 63x/1.4 N.A. Plan Apochromat objective and Zeiss Axiovision software. Individual tiles were stitched together using the Fiji plug-in MetaStitch (generously provided by Dr. Stephen Smith, Stanford University) into section mosaics, and compiled into volumetric stacks. Volume renderings based on these aligned mosaics were used to verify accurate alignment (Supplemental Movies S1 and S2), after which the aligned stacks were imported as serial sections into Reconstruct (Fiala, 2005) for spine quantification. No adjustments were made to the brightness/contrast of raw images for data analysis. For renderings, which are included in Figure S1 only for illustrative purposes, brightness and contrast were adjusted when needed to extract subtle morphological information. All proximal dendritic segments originated from dendritic branches at least 50 μm away from the soma; their distal counterparts, from the same individual dendrites, were at least 140 μm from the soma. Middle segments of the dendrites were at least 20 μm from either the distal or the proximal segment.

Unbiased Quantitative Electron Microscopy

Five young adult (6 months old) male F1 hybrid Fisher344 x Brown Norway rats (Harlan, Indianapolis, IN) were intracardially perfused with a mixture of paraformaldehyde and glutaraldehyde. Tissue samples were prepared for conventional electron microscopy and used to determine the total number of axospinous and perforated and nonperforated synapses in the dorsal half of the hippocampus with unbiased stereological sampling and counting procedures combined with serial section analyses (Nicholson et al., 2006). The right hippocampal formation was dissected free, and its dorsal half was cut into five to seven consecutive transverse slabs. The location of the first cut was chosen randomly within the most rostral 0.8 mm interval, and subsequent cuts were made systematically at 0.8 mm intervals. From the rostral face of the slab, a 1 μm-thick histological section was prepared and stained with azure II/methylene blue. CA1 was distinguished from adjacent CA2 and subiculum by the presence of a relatively narrow stratum pyramidale comprising tightly packed pyramidal cell bodies of homogeneously small size (Amaral and Lavenex, 2006; Ishizuka et al., 1995). Within CA1, the boundaries of SO were determined by stratum pyramidale and the alveus, the latter identifiable by the high density of myelinated fibers. Within CA1 SO, the proximal (pSO), middle (mSO), and distal (dSO) regions were defined as lying within the first, middle, and last third of the total width of SO measured along the stratum pyramidale-alveus axis. The area of SO was estimated in each section by using ImageJ. The total volume of CA1 SO was calculated as the product of their summed profile areas and the average thickness of the polymerized tissue slabs. This volume divided by three yielded the volumes of pSO,

mSO, and dSO.

Slabs from each rat were chosen in a systematic random manner, trimmed, and cut to yield ribbons of 24 to 39 serial ultrathin (68 nm) sections (from each slab). For pSO and dSO, five slabs were chosen for three of the rats and four slabs for the other two rats (23 slabs total). For mSO, five slabs were chosen from three rats (15 slabs total). Each section spanned the extent of the CA1 basal dendritic region, from the pyramidal cell layer to the alveus. The borders of pSO, mSO, and dSO were determined from measurements performed on the histological sections using the field delineator of the electron microscope. Subsequently, electron micrographs of a systematic randomly selected sampling field were imaged from each SO sub-region on the same set of serial sections. In each rat, the total number of perforated and nonperforated synapses was estimated separately for the pSO, mSO, and dSO regions as the product of the region volume (in μm^3) and the averaged synaptic numerical density (synapses/μm^3) obtained from all slabs. Synaptic numerical density was determined with the physical disector, using 18 consecutive disectors in the middle of each series. Examination of micrographs taken within the alveus (beyond dSO) showed an absence of identifiable synaptic PSDs in the region. The data included 498 perforated and 6338 nonperforated synapses. Regional differences in perforated synapse number, nonperforated synapse number, and the ratio of perforated to nonperforated synapses were assessed using ANOVA.

Quantification of AMPAR and NMDAR immunoreactivity

Postembedding immunogold electron microscopy was used to assess the expression of postsynaptic AMPARs and NMDARs in 3 young adult hybrid Fisher344 x Brown Norway, as specified previously (Nicholson et al., 2006; Nicholson and Geinisman, 2009). Briefly, the conventional EM sampling design was used, with the following modifications. The dorsal half of the right hippocampal formation was cut into transverse 0.3 mm thick slabs. Four slabs were selected in a systematic random manner, and the CA1 region in each was divided along its mediolateral extent into three slivers, each of which was 0.5-1 mm in width. Following plunge freezing, freeze substitution, and low-temperature embedding in Lowicryl (Electron Microscopy Sciences), one sliver from each slab was used to prepare 15 to 30 serial ultrathin (67 nm) sections (four slivers per rat; 12 slivers total). The latter were immunostained with a mixture of primary antibodies (Chemicon) specific to either AMPAR subunits (GluR1, GlurR2, GluR2/3, and GluR4) or NMDAR subunits (NR1 and NR2A/B), and then with secondary antibodies conjugated to 10 nm gold particles (British BioCell International). Electron micrographs were obtained from systematic randomly selected fields in pSO, mSO, and dSO in the same serial sections. The number of particles per synapse, PSD area, and particle density per PSD unit area (μm^2) were estimated from measurements on serial sections. For the parent dendrite-caliber analyses, synapses were followed through serial sections. If the connection between the parent spine and its parent dendrite was captured, parent dendrite diameter was measured in 3 different locations and averaged.

The data comprised 154 perforated and 2723 nonperforated immunopositive synapses for the AMPAR immunostaining, and 131 perforated and 1211 nonperforated immunopositive synapses for the NMDAR

immunostaining. Regional differences in particle number were assessed using a Multivariate Analysis of Covariance (MANCOVA), with the region and synapse subtype as categorical predictors and the PSD area as the covariate. For the analyses parent dendrite-caliber analyses, the data are comprised of 760 immunopositive axospinous synapses, of which 357 were perforated and 403 were nonperforated.

Data Adjustment

Morphological analyses (Megías et al., 2001), corroborated by our own observations, indicate that there are very few basal axospinous synapses on branch segments within ~50μm of the soma. Based on the experimental protocol, pSO was defined as the region lying within 60 μm of the soma, mSO as the region between 60 μm and 120 μm from the soma, and dSO the region lying beyond 120 μm from the soma. These distances are measured along the perpendicular axis joining stratum pyramidale and SO, not in terms of dendritic distance. In terms of individual dendrites, we calculated the distribution of 5 μm-long individual dendritic segments as a function of distance from the soma. To identify the boundaries separating proximal, middle, and distal branch segments, we divided the distribution into terciles. Using this analysis, we defined proximal branch segments as those lying between 50 μm and 110 μm from the soma, middle branch segments as those lying between 110 μm and 160 μm from the soma, and distal segments as those lying beyond 160 μm from the soma. Due to the quasi-hemispherical distribution of branches in SO (Figure 2B), there are middle and distal branch segments in pSO and proximal and distal segments in mSO. After quantifying the proportion of these segments in each region (Figure 2B), we adjusted a given measure (synapse number, particle number, particle density) by solving the following system of equations:

$$x_{pSO}=(f_{proximal\ in\ pSO})(y_{pSO})+(f_{middle\ in\ pSO})(y_{mSO})+(f_{distal\ in\ pSO})(y_{dSO})$$

$$x_{mSO}=(f_{proximal\ in\ mSO})(y_{pSO})+(f_{middle\ in\ mSO})(y_{mSO})+(f_{distal\ in\ mSO})(y_{dSO})$$

$$x_{dSO}=(f_{proximal\ in\ dSO})(y_{pSO})+(f_{middle\ in\ dSO})(y_{mSO})+(f_{distal\ in\ dSO})(y_{dSO})$$

where f indicates the fraction of proximal, middle, or distal segments in the relevant region (pSO, mSO, or dSO), x represents the experimentally observed value, and y represents the adjusted value to be solved for. For the synapse number estimates obtained through conventional electron microscopy (Figure 2E), the adjusted values were synaptic numerical density measurements, and each equation was multiplied by the region-specific total dendritic length.

The radial nature of the basal dendritic arborization required us to correct for the consequent presence of distal dendrites in both pSO and mSO, and middle segments in pSO (no correction was needed for data from dSO; Figure 2B). Importantly, such corrections had little effect on the outcome of any of the analyses. For example, the uncorrected AMPAR particle numbers for perforated synapses from pSO, mSO, and dSO were (average ± SEM) 9.54 ± 0.82, 11.91 ± 1.01, and 12.43 ± 0.76, respectively. The uncorrected NMDAR particle numbers for perforated synapses from pSO, mSO, and dSO were (average ± SEM) 7.33 ± 0.77, 6.05 ± 0.55, and 6.08 ± 0.82, respectively. Comparisons of AMPAR and NMDAR data from pSO and dSO via t-tests still

yield significant differences at $p < 0.05$, underscoring our intent to provide an empirically corrected estimate of synapse number and receptor expression, while preserving the power of our approach.

Computational modeling

The CA1 pyramidal neuron model used in all simulations was reconstructed from a stained neuron in a hippocampal slice as described previously (Golding et al., 2005). All simulations were carried out using the NEURON simulation environment (Hines and Carnevale, 1997). The model included passive membrane properties (capacitance and resistance) and active sodium (Na), delayed-rectifier potassium (KDR), A-type potassium (KA), and H-channels (Ih). Passive properties were constrained by electrophysiological recording of voltage attenuation from the soma to the dendrite in the reconstructed neuron (Golding et al., 2005). The active Na, KDR, and KA conductances were all held constant throughout the basal dendritic tree. Ih conductance was distributed sigmoidally in the apical tree and uniformly in the basal tree. For the distance-based simulations in Figures 4 and 5, the data points for the linear equations line up with the AMPAR- and NMDAR-mediated conductances based on particle numbers for pSO, mSO, and dSO (Figure 3), corresponding to distances of 80, 135, and 185 μm from the soma. For the diameter-based simulations in Figure 6, the AMPAR- and NMDAR-mediated conductance values for thick, medium, and thin dendrites line up with the values for dendrites with diameters of 750, 550, and 350 nm, respectively.

AMPAR-mediated excitatory conductances were modeled as a difference of two exponentials, with a rise time constant of 0.2 ms, decay time constant of 3 ms, and a reversal potential of 0 mV. NMDAR-mediated excitatory conductances were modeled as a difference of two exponentials, with a rise time constant of 2 ms, a decay time constant of 86 ms, a reversal potential of 0 mV, and voltage-dependence as characterized by Jahr and Stevens (1990). Dendritic spikes were identified by a nonlinear jump in the local dendritic voltage. All synapses were placed on simulated spines whose total neck resistances were 500MΩ. All models will be made available on the authors' website (http://dendrites.esam.northwestern.edu/).

To convert particle numbers from the experimental data to conductance values, we determined the conductance necessary for a perforated synapse on a proximal dendrite to generate a somatic EPSP of ~0.2 mV, and then divided this conductance by the average number immunogold particles for perforated synapses in pSO, yielding the conductance of a single immunogold particle. This "$g_{particle}$" was then scaled accordingly for perforated synapses in the different regions, but kept constant for nonperforated synapses in accordance with our experimental observations. NMDAR conductance was determined by matching experimentally observed ratios between unitary AMPAR-mediated and NMDAR-mediated currents (Myme et al., 2003), and then scaled similarly according to immunogold particle number for the synaptic subtypes in the different dendritic regions. Each AMPAR immunogold particle corresponded to a conductance of 70 pS, and each NMDAR immunogold particle corresponded to a conductance of 60 pS. Dendritic spikes were identified by a nonlinear jump in the local dendritic voltage. All synapses were placed on simulated spines whose total neck resistances were 500MΩ.

For the experimentally observed synapse distribution case in Figure 4, perforated synaptic weights were calculated as linear gradients whose midpoint values corresponded to the immunogold electron microscopy particle counts observed experimentally in pSO, mSO, and dSO. The correspondence between AMPA particle number and conductance was chosen to match those used in previous studies (Nicholson et al., 2006). The value for single-channel NMDA conductance was selected to match experimentally observed ratios between unitary AMPA and NMDA currents (Otmakhova et al., 2002, Myme et al., 2003). The locations of nonperforated synapses were randomly drawn from a linearly decreasing density distribution starting from 5.5 synapses/μm near the soma and declining to 0.5 synapses/μm at branch segments 250 μm from the soma. In the uniform distribution case, perforated conductances were set at the middle values from the non-uniform case, and all synapse locations were drawn from a uniform distribution. It is worth noting that there was one dendritic branch where distal perforated synapses generated lower amplitude somatic EPSPs than proximal ones, even with the experimentally observed conductance distribution. Morphologically, this branch was distinct in two ways: its diameter did not taper with distance from the soma, and it had no terminal end, bifurcating instead into two daughter branches. This suggests that the normalization due to the observed synaptic strength variations is most effective on dendrites with tapering diameters and terminal ends, which form the majority of basal and apical oblique dendrites. Despite this, the experimentally observed scaling of AMPARs and NMDARs still preserves the normalization of somatic EPSPs and NMDAR-mediated current flow when diameter is held constant (not shown) or if diameter is determined from the electron microscopic tissue (Figure S4). For Figure S4, the primary apical dendrite diameter in the reconstructed neuron was adjusted using the linear interpolation of the EM-measured diameter values as a function of distance. For the apical oblique dendrites, the dendritic diameter at the proximal end was left unchanged from the optical reconstruction, whereas the middle and distal segment diameters were tapered using linearly interpolated values ranging from the EM measurements for proximal and distal oblique diameters (shown in Figure 1). For all multi-synapse simulations, all synapses were activated synchronously.

For simulations using diameter-based synaptic conductances (Figure 6), particle counts were interpolated linearly between the experimentally observed values for thick (750 nm), medium (550 nm), and thin (350 nm) diameter dendrites. The conductance for a given synapse was thus calculated by multiplying the assumed particle number (based on parent dendrite thickness, as shown in Figures 6C,D) by the conductance per particle ($g_{particle}$, as described in the text). Though the values for EPSPs in the color shape-plots for Figure 6 show between-dendrite variability, it is important to note that the experimentally observed case shows very little within-dendrite variability. The between-dendrite variability is due to the fact that a synapse on a 350 nm dendrite was always assigned the same conductance, regardless of whether its location was 100 μm or 400 μm from the soma. Thus, normalizing the distal values to the proximal values captures the location-independence of EPSPs and NMDAR-mediated current flow conferred by the experimentally observed synapse and ion channel gradients.

Supplemental References

Ferris, A.M., Giberson, R.T., Sanders, M.A., and Day, J.R. (2009). Advanced laboratory techniques for sample processing and immunolabeling using microwave radiation. J. Neurosci. Methods *182*, 157-164.

Megías, M., Emri, Z., Freund, T.F., and Gulyas, A.I. (2001). Total number and distribution of inhibitory and excitatory synapses on hippocampal CA1 pyramidal cells. Neuroscience *102*, 527-540.

Micheva, K.D., Busse, B., Weiler, N.C., O'Rourke, M., and Smith, S.J. (2010). Single-synapse analysis of a diverse synapse population: proteomic imaging methods and markers. Neuron *68*, 639-653.

Myme, C.I.O., Sugino, K., Turrigiano, G.G., and Nelson, S.B. (2003). The NMDA-to-AMPA ratio at synapses onto layer 2/3 pyramidal neurons is conserved across prefrontal and visual cortices. J. Neurophysiology *90*, 771-779.

Otmakhova, N.A., Otmakhov, N., and Lisman, J. (2002). Pathway-specific properties of AMPA and NMDA-mediated transmission in CA1 hippocampal pyramidal cells. J. Neurosci. *15*, 1199-1207.